inorganics

MDPI

Article

Unveiling the Electrocatalytic Performances of the Pd-MoS_2 Catalyst for Methanol-Mediated Overall Water Splitting

Aviraj M. Teli [1,†], Sagar M. Mane [2,†], Rajneesh Kumar Mishra [3,*], Wookhee Jeon [4] and Jae Cheol Shin [1,*]

[1] Division of Electronics and Electrical Engineering, Dongguk University-Seoul, Seoul 04620, Republic of Korea; avteli.teli@gmail.com
[2] Department of Fiber System Engineering, Yeungnam University, 280 Dehak-Ro, Gyeongsan 38541, Gyeongbuk, Republic of Korea; manesagar99@gmail.com
[3] Department of Physics, Yeungnam University, Gyeongsan 38541, Gyeongbuk, Republic of Korea
[4] Department of Semiconductor, Convergence Engineering, Sungkyunkwan University, Suwon 16419, Gyeonggi, Republic of Korea; wookie92@skku.edu
* Correspondence: rajneeshmishra08@gmail.com (R.K.M.); jcshin@dgu.ac.kr (J.C.S.)
† These authors contributed equally to this work.

Abstract: Herein, this work elucidates the synthesis of the Pd-MoS_2 catalyst for application in methanol-mediated overall water splitting. The scanning electron microscope (SEM) and transmission electron microscope (TEM) pictures offer an exciting nanostructured shape of the Pd-MoS_2, depicting a high surface area. Further, high-resolution TEM (HRTEM) pictures confirm the lattice plane (100), lattice spacing (0.26 nm), and hexagonal crystal structure of the Pd-MoS_2. Moreover, high-angle annular dark-field (HAADF) images and related color maps disclose the Mo, S, and Pd elements of the Pd-MoS_2. The Pd-MoS_2 catalyst exhibits lower overpotentials of 224.6 mV [methanol-mediated hydrogen evolution reaction (MM-HER)] at -10 mA cm^{-2} and 133 mV [methanol-mediated oxygen evolution reaction (MM-OER)] at 10 mA cm^{-2}. Further, the Pd-MoS_2 illustrates noteworthy stability for 15.5 h for MM-HER and 18 h for MM-OER by chronopotentiometry test. Excitingly, the Pd-MoS_2||Pd-MoS_2 cell reveals a small potential of 1.581 V compared to the MoS_2||MoS_2 cell (1.648 V) in methanol-mediated overall water splitting. In addition, the Pd-MoS_2||Pd-MoS_2 combination reveals brilliant durability over 18 h at 10 mA cm^{-2}.

Keywords: Pd-MoS_2; methanol-mediated hydrogen evolution reaction; methanol-mediated oxygen evolution reaction (MM-OER); methanol-mediated overall water splitting; outstanding stability

check for updates

Academic Editor: Ting Deng

Received: 24 December 2024
Accepted: 13 January 2025
Published: 15 January 2025

Citation: Teli, A.M.; Mane, S.M.; Mishra, R.K.; Jeon, W.; Shin, J.C. Unveiling the Electrocatalytic Performances of the Pd-MoS_2 Catalyst for Methanol-Mediated Overall Water Splitting. *Inorganics* **2025**, *13*, 21. https://doi.org/10.3390/inorganics13010021

1. Introduction

Currently, the rising global population and fast industrialization have led to record energy consumption, blinking a keen interest in future energy sources [1]. Fascinatingly, fossil fuels are a main energy source for industry, irrigation, and transportation, contributing to critical environmental challenges, such as pollution and greenhouse gas emissions [2]. Therefore, these issues highlight the necessity to transition toward sustainable, green, and clean energy sources [3]. Remarkably, hydrogen is a hopeful clean energy source that has the potential to transform energy systems, offering a sustainable substitution for fossil fuels due to its high energy, which could considerably reach carbon neutrality and eco-friendly combustion and mitigate climate change impacts [4]. Intriguingly, electrochemical water splitting is a scalable, effective, and simple technique for hydrogen energy production involving the decomposition of water (H_2O) into oxygen (O_2) and hydrogen (H_2) [5]. Attractively, the overpotentials and Tafel slopes mainly affect the hydrogen and

oxygen productivity during the electrochemical water splitting, which is very important for hydrogen and oxygen generation [6]. Recently, methanol-mediated hydrogen evolution, methanol-mediated oxygen evolution reaction (MM-OER), and methanol-mediated overall water splitting have extended significant attention due to more efficient alternatives to traditional water splitting [7]. Combining methanol (CH_3OH) into the KOH electrolyte during the electrochemical water splitting process can lower the energy barrier for hydrogen energy production [8]. Excitingly, it can considerably decrease the overpotential, thereby reducing the energy input for hydrogen energy production. Interestingly, this approach opens new pathways for using methanol, which can be produced sustainably from biomass or captured carbon dioxide, further enhancing the environmental benefits [9]. Furthermore, methanol-mediated processes present a captivating alternative that could improve efficiency and stability for sustainable energy generation. Various Pt-based nanomaterials are currently used for hydrogen evolution reactions [10,11]. However, ruthenium and iridium-based nanomaterials are utilized for oxygen evolution reactions [12,13]. Amusingly, their expensive nature and scarcity in the crust of the earth limit their possible usage as catalysts for sustainable and commercial hydrogen generation. Therefore, it is necessary to develop cutting-edge, low-cost catalysts operating at lower overpotentials while maintaining high durability, a prerequisite for a hydrogen energy-based economy, addressing energy demands and environmental sustainability for future generations.

Transition metal dichalcogenides (TMDs) illustrate a family of two-dimensional (2D) layered structures through the well-known MX_2 formula, in which X is a chalcogen (such as S, Se, and Te) and M is a transition metal (such as Mo, W, and Ti) [14]. In addition, TMDs reveal exclusive electronic, optical, and magnetic characteristics due to their typical 2D nature. The 2D layers of the TMDs are attached by weak van der Waals forces [15]. MoS_2 comprises hexagonally packed Mo atoms between two layers of S atoms [16]. Additionally, TMDs have gained significant consideration for their vibrant applications in several fields, such as electronics, optoelectronics, and catalysis, making them a crucial theme of research in materials science and nanotechnology [17,18]. Therefore, monolayer MoS_2 endows a direct optical band gap of approximately 1.8 eV, making it suitable for optoelectronic device fabrication [19]. Additionally, MoS_2 exhibits excellent mechanical flexibility, high chemical stability, and strong spin-orbit [20]. The MoS_2's fashionable characteristics offer its research in various applications, such as transistors, sensors, and flexible electronic devices, because of its high carrier mobility and scalability [21]. Also, MoS_2 is demonstrated as an exciting catalyst for hydrogen generation reactions and other electrochemical processes [22]. Additionally, MoS_2's optical properties are harnessed in photodetectors and light-emitting devices [23,24]. The MoS_2 is synthesized through various physical and chemical methods, each offering distinct advantages. Further, the high-quality MoS_2 monolayers are produced using the mechanical exfoliation method by peeling off layers from bulk crystals [25]. In addition, the MoS_2 thin films are developed on many substrates by chemical vapor deposition (CVD), which allows for large-area, scalable, and uniform thin films for various commercial applications [26]. Moreover, the Mo and S precursor solution react under controlled temperature and pressure, yielding tunable morphology and properties of the MoS_2 using the hydrothermal and solvothermal methods [27,28]. Further, the MoS_2 can be found in various morphologies depending on the synthesis method and conditions, including nanosheets [29], nanorods [30], nanotubes [31], nanowires [32], nanoflowers [33], and quantum dots [34]. Fascinatingly, two-dimensional MoS_2 nanosheets are the most common form, offering large surface areas and high aspect ratios. On the other hand, three-dimensional MoS_2 nanotubes and nanoflowers deliver unique morphological topographies, which can enhance electrocatalytic activities. Interestingly, zero-dimensional MoS_2 quantum dots are generally suitable in optoelectronic applications due to their size-

tunable optical and electronic properties [35]. Moreover, the MoS_2 nanomaterial is used in batteries, fuel cells, and supercapacitors because of its high capacity and stability [36–38]. Interestingly, MoS_2 is also used in water purification and sensing in ecological applications because of its high reactivity and large surface area [39,40]. Fascinatingly, the MoS_2 enables its use in drug delivery and cancer therapy due to its biocompatibility and photothermal properties [41,42]. However, the 2D layered MoS_2 emphasizes its potential applications in advanced technologies due to its multifunctional nature. Therefore, tuning the structural and morphological properties of the MoS_2 by doping or constructing heterostructures has been significantly studied, which offers enhanced performance in different applications. Fascinatingly, Pd doping in the MoS_2 can alter the electronic properties and create more active sites, facilitating greater adsorption and dissociation of water electrolysis during methanol-mediated overall water splitting, which makes it a highly effective catalyst for sustainable hydrogen energy generation.

In this paper, we studied the methanol-mediated hydrogen evolution reaction (MM-HER), methanol-mediated oxygen evolution reaction (MM-OER), and methanol-mediated overall water splitting (MM-OWS) of the Pd-doped MoS_2 (Pd-MoS_2) catalyst, which is a promising 2D nanomaterial for sustainable hydrogen generation through electrocatalytic water splitting. Interestingly, the presence of methanol with the KOH electrolyte works as a co-reactant, significantly boosting the electrocatalytic activities of the methanol-mediated overall water splitting, facilitating the adsorption process and also supporting to alleviate the transitional active sites on the surface of the Pd-MoS_2 electrocatalyst, thereby enhancing the rate of reaction kinetics. Fascinatingly, it is observed that the Pd-MoS_2 catalyst illustrates outstanding catalytic performances and excellent stability. The Pd-MoS_2‖Pd-MoS_2 cell elucidates a lower potential of 1.581 V and tremendous durability throughout 18 h at 10 mA cm^{-2}. Therefore, it is concluded that the Pd-MoS_2 catalyst can be an excellent nanomaterial for hydrogen energy generation for commercial applications.

2. Results and Discussion

Figure 1a elucidates the XRD patterns of the Pd-doped MoS_2 and MoS_2. It is observed that the XRD spectra illustrate the lattice planes (002), (101), and (110) to MoS_2 and Pd-doped MoS_2. Therefore, it is concluded that the XRD patterns suggest the fruitful preparation of the MoS_2 and Pd-doped MoS_2, which is well matched with the JCPDS card No. 37-1492 [43]. Further, an XPS study was executed to examine the chemical composition of the Pd-doped MoS_2. Figure 1b–d elucidate the XPS patterns of the Pd-doped MoS_2 nanostructure. Figure 1b depicts the XPS patterns of Mo 3d peaks, which illustrates the various peaks such as Mo^{4+} $3d_{5/2}$ (228.72 eV), Mo^{4+} $3d_{3/2}$ (231.85 eV), and Mo^{6+} $3d_{3/2}$ (234.88 eV). Figure 1c portrays the XPS spectrum of the S 2p peaks, revealing S^{2-} $2p_{5/2}$ at 161.45 eV and S^{2-} $2p_{1/2}$ at 162.83 eV. In addition, the observed Pd 3d peaks are Pd^0 $3d_{5/2}$ (335.5 eV), Pd^{2+} $3d_{5/2}$ (337.7 eV), Pd^0 $3d_{3/2}$ (340.56 eV), and Pd^{2+} $3d_{3/2}$ (342.2 eV). Similar reports on MoS_2 have been discussed in the literature, which justifies our XPS results [44–46]. Therefore, it is determined that the XPS patterns approve the successful synthesis of the Pd-doped MoS_2.

Figure 2a,b reveal the SEM of the MoS_2 at 2 μm and 1 μm scales. It shows the layered sphere-like morphology of the MoS_2. Figure 2c,d display the SEM of the Pd-doped MoS_2 at different locations and magnifications. The SEM pictures in Figure 2c,d provide detailed insights into the morphology of Pd-doped MoS_2 nanolayers grown on Ni foam. Figure 2c elucidates the SEM image at a 5 μm scale to explore the large view of the Pd-MoS_2. Further, Figure 2d depicts the SEM image at a 2 μm scale of the Pd-MoS_2. It is observed that the Pd-MoS_2 deposited on the Ni-foam shows very thin layers. Interestingly, Pd doping may significantly influence the crystallinity, uniformity, and fine-edge nanolayer of the Pd-MoS_2.

Moreover, various features such as growth conditions, synthesis temperature, time, doping concentration, and annealing process also play vital roles in shaping the morphology of the MoS_2 [47,48]. Amazingly, it is apparent from SEM morphologies that the Pd-MoS_2 offers a high surface area and wrinkled nanolayers, which can be beneficial for methanol-mediated hydrogen, oxygen evolution, and methanol-mediated overall water splitting. Likewise, the shape of the Pd-MoS_2 and MoS_2 are also discussed using the TEM. Figure 3a–c divulge the TEM morphologies of Pd-MoS_2 at 50 nm, 10 nm, and 5 nm scale bars, respectively. Figure 3d–f unveil the TEM pictures of Pd-MoS_2 at 100 nm, 50 nm, and 10 nm scale bars, respectively. Figure 3d discloses the TEM pictures at a 100 nm scale bar to discover the morphology and layer shape of the Pd-MoS_2. Figure 3e,f illustrate the even higher magnification TEM images at 50 nm and 10 nm scales to check the layer bending and layers overlapping on each other. Interestingly, it is also observed from TEM that the Pd-MoS_2 nanolayers are stacked or slightly exfoliated, which is vital for applications depending on surface interactions, such as methanol-mediated overall water splitting. Interestingly, these TEM images at different scales collectively enhance the understanding of the structural properties of the Pd-MoS_2, indicating the successful synthesis of the Pd-MoS_2 nanomaterial and its potential applicability in methanol-mediated oxygen, hydrogen evolution, and methanol-mediated overall water splitting.

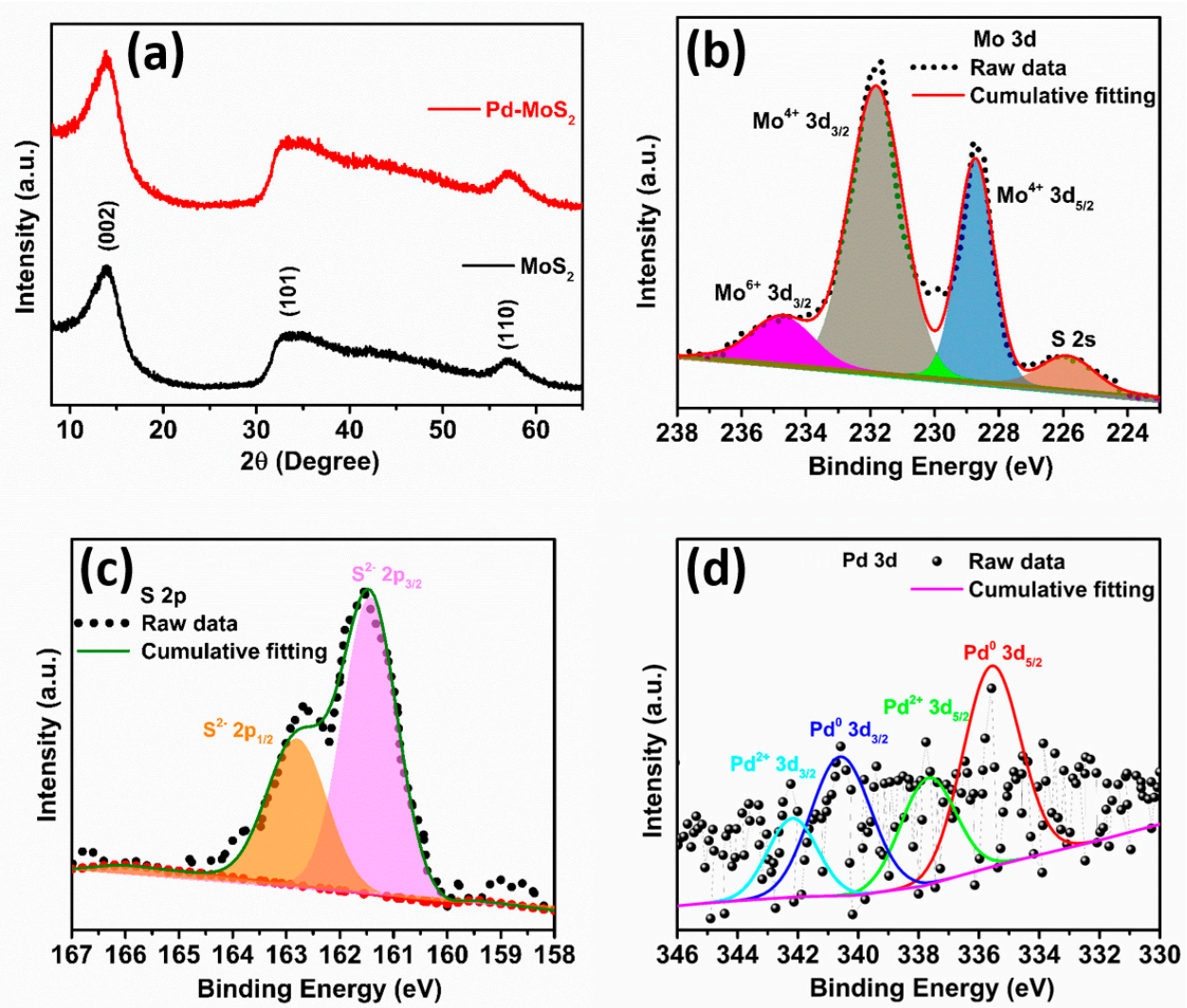

Figure 1. (**a**) XRD results of MoS_2 and Pd-MoS_2. XPS results of the (**b**) Mo 3d, (**c**) S 2p, and (**d**) Pd 3d peaks of Pd-MoS_2.

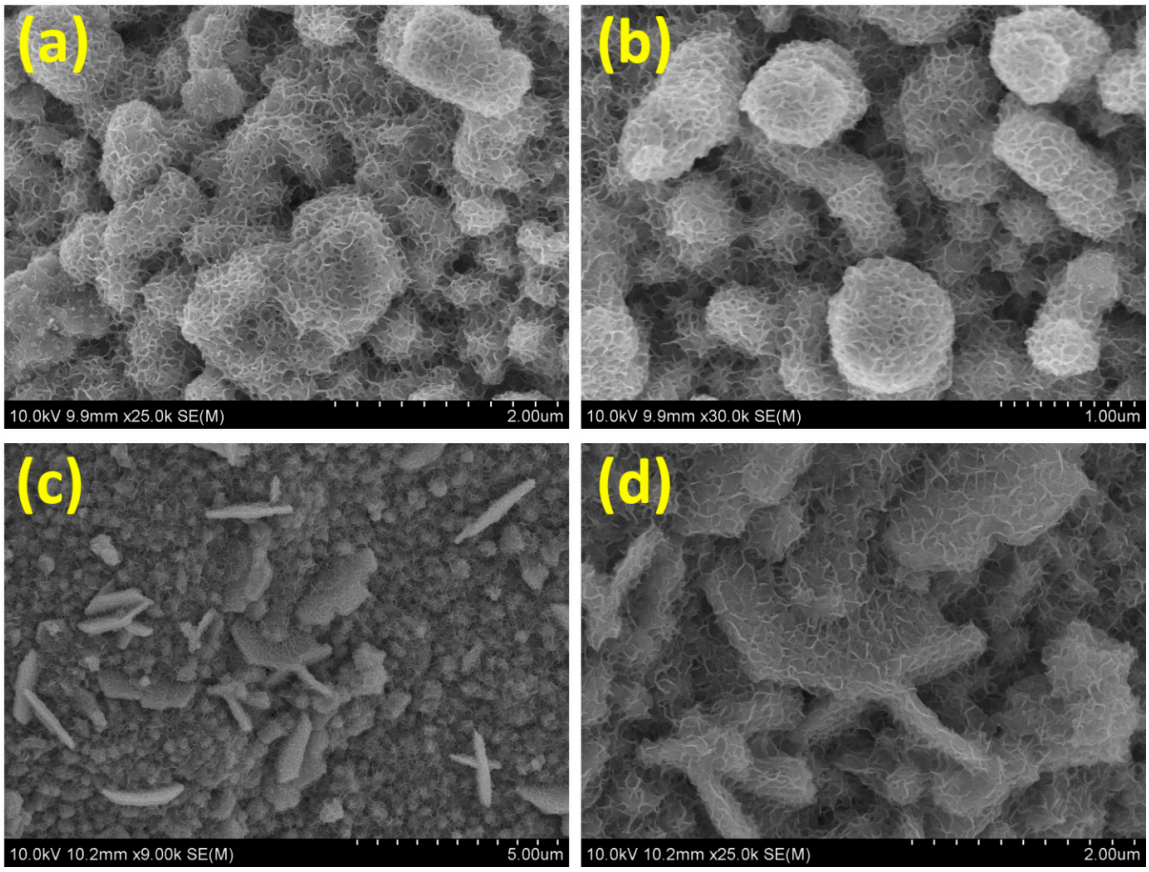

Figure 2. SEM pictures of the (**a**,**b**) MoS_2 and (**c**,**d**) Pd-MoS_2.

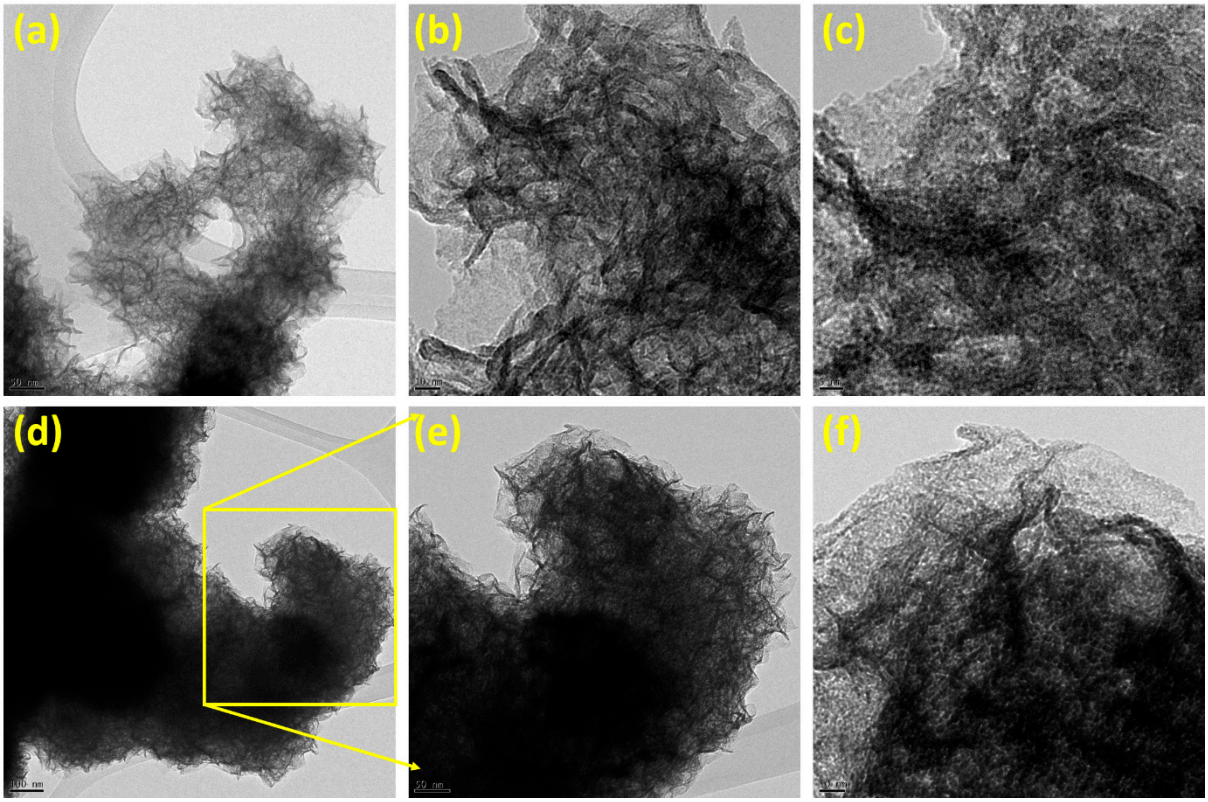

Figure 3. TEM pictures of the MoS_2 at a scale bar of (**a**) 50 nm, (**b**) 10 nm, and (**c**) 5 nm. TEM pictures of the Pd-MoS_2 at a scale bar of (**d**) 100 nm, (**e**) 50 nm, and (**f**) 10 nm.

In addition, the high-resolution transmission electron microscope (HRTEM) pictures and fast Fourier transform (FFT) pictures deliver a comprehensive indulgence of the structural features of Pd-MoS_2. Figure 4a–e unveil the HRTEM pictures, magnified HRTEM images, and FFT patterns of the Pd-MoS_2. Figure 4a portrays the HRTEM images of Pd-MoS_2, illustrating various crystallites with lattice fringes. Figure 4b,d describe the enlarged portion of the HRTEM image to measure and discuss the lattice spacings of the Pd-MoS_2. It is seen from HRTEM images that the lattice spacing of Pd-MoS_2 is 0.26 nm. Furthermore, Figure 4c,e define the FFT pattern of Pd-MoS_2 from the selected area, as revealed in Figure 4b,d. FFT patterns illustrate the lattice planes (100) of the Pd-MoS_2. Interestingly, the accuracy and uniqueness of the lattice fringes and FFT patterns suggest a high-quality synthesis of the Pd-MoS_2. Remarkably, the HRTEM and FFT results of the Pd-MoS_2 show the successful synthesis of the hexagonal crystal phase and are well coordinated with the JCPDS card no. 37-1492 [49]. In addition, we studied the elemental analysis of Pd-MoS_2 using elemental mapping. Figure 5 exhibits the HAADF result and analogous color maps of the Pd-MoS_2, which shows the elemental mappings corresponding to Mo, S, and Pd elements, providing a spatial distribution of these elements of the Pd-MoS_2. Combining the HAADF image and the elemental mappings offers compelling evidence that Pd-MoS_2 was successfully synthesized via the solvothermal method. Figure 5a designates the high-angle annular dark field (HAADF) outcome of Pd-MoS_2. Figure 5b,c portray the elementals of Mo and S of the Pd-MoS_2 from the HAADF image (Figure 5a). The Pd element mapping is vital for confirming the doping of Pd into the Pd-MoS_2 structure, as exposed in Figure 5d.

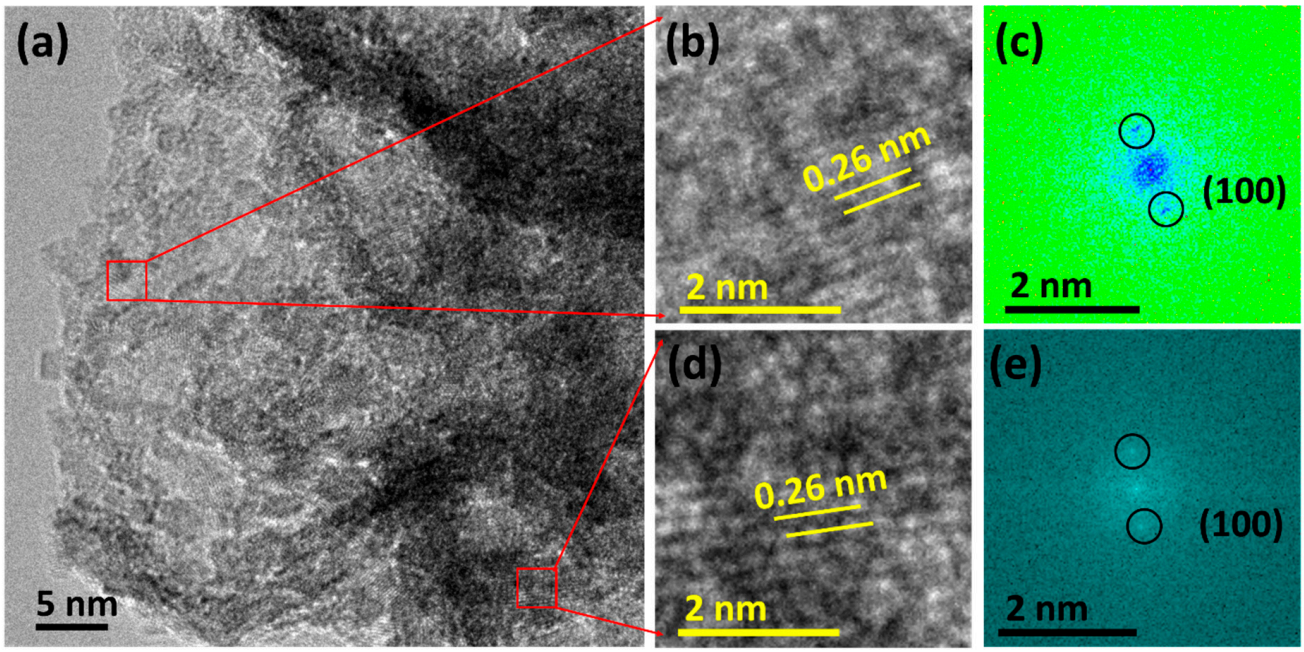

Figure 4. (**a**) HRTEM picture, (**b**,**d**) HRTEM pictures of the selected locations, and the (**c**,**e**) FFT images of the Pd-MoS_2.

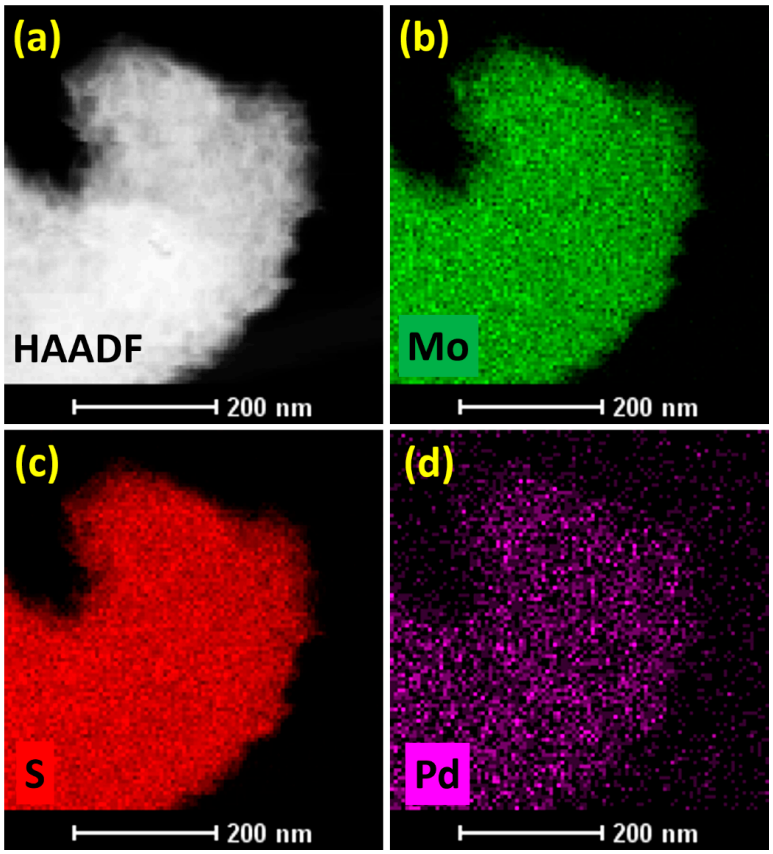

Figure 5. (**a**) HAADF picture and color maps of (**b**) Mo, (**c**) S, and (**d**) Pd of Pd-MoS_2.

The methanol-mediated oxygen evolution reaction (MM-OER) is a significant electrochemical procedure for fuel cells. Figure 6 illustrates the MM-OER of the MoS_2 and Pd-MoS_2 electrocatalysts at 5 mV s^{-1} in 1 M methanol + 1 M KOH. Figure 6a shows the LSV results of the Pd-MoS_2 and MoS_2 electrocatalysts at 5 mV s^{-1} for the MM-OER. It is seen that the Pd-MoS_2 electrocatalyst unveils superior electrocatalytic performance for the MM-OER compared to the pure MoS_2 electrocatalyst. Furthermore, the current density defines the maximum current achieved during the MM-OER for the MoS_2 and Pd-MoS_2 catalysts. In addition, higher peak current densities designate higher electrocatalytic MM-OER activities, signifying that the Pd-MoS_2 electrocatalyst can facilitate a better MM-OER rate than the pure MoS_2 electrocatalyst. Further, the inset in Figure 6a illustrates the low-scale results of LSV for Pd-MoS_2 and MoS_2 catalysts for MM-OER to elucidate the trends near the 10 mA cm^{-2}. Figure 6b displays the overpotentials of MoS_2 and Pd-MoS_2 catalysts for MM-OER at 10 mA cm^{-2}. The observed overpotentials of the Pd-MoS_2 and MoS_2 are 133 mV and 160 mV at 10 mA cm^{-2}, respectively. Stimulatingly, palladium (Pd) in Pd-MoS_2 is recognized for its brilliant electrocatalytic properties in MM-OER, which can enable the adsorption and activation of methanol and other intermediates more effectively than the MoS_2 catalyst [50]. Figure 6c exhibits the Tafel curves of MoS_2 and Pd-MoS_2 catalysts for MM-OER. The Pd-MoS_2 and MoS_2 electrocatalysts divulge the Tafel slopes of 112 mV dec^{-1} and 148 mV dec^{-1}, respectively. Captivatingly, the Tafel slope delivers insight into the rate-determining process and the efficiency of Pd-MoS_2 and MoS_2 catalysts in promoting the kinetics of MM-OER. Interestingly, the Pd-MoS_2 is a more efficient catalyst for MM-OER than pure MoS_2, supported by its lower Tafel slope, as revealed in Figure 6c. In addition, the low Tafel slope of the Pd-MoS_2 catalyst elucidates faster MM-OER reaction kinetics and a more effective electrocatalytic process, attributing to the advantageous effects of Pd doping. Further, Figure 6d displays the LSV plots of the Pd-MoS_2 at 5 mV s^{-1}, which

depicts 157 mV, and 133 mV overpotential without and with methanol-mediated OER at 10 mA cm^{-2}, respectively. Therefore, it is concluded that methanol played a decisive role in the reduction in overpotentials during methanol-mediated OER. Figure 6e interprets the EIS plots of the MoS_2 and Pd-MoS_2 at respective overpotentials of MM-OER, which depicts the small series and charge-transfer resistance of the Pd-MoS_2 compared with MoS_2. Figure 6f unveils the stability results of the Pd-MoS_2 catalyst during MM-OER throughout 18 h at 10 mA cm^{-2}. Further, it is perceived that the Pd-MoS_2 catalyst performs consistently better for 18 h, suggesting its resilience and competence for long-term use without degradation in MM-OER application at 10 mA cm^{-2}.

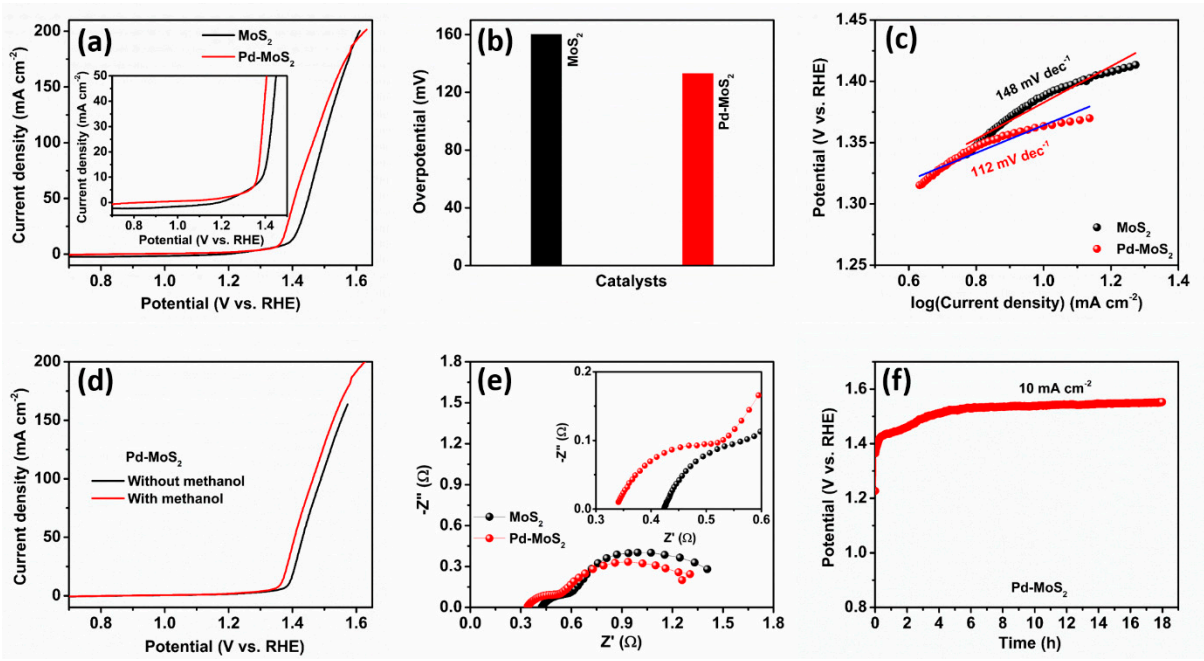

Figure 6. Electrocatalytic methanol-mediated OER. (**a**) LSV results, (**b**) overpotential graphs, and (**c**) Tafel graphs of the Pd-MoS_2 and MoS_2 electrocatalysts. (**d**) LSV curves of the Pd-MoS_2 without and with methanol. (**e**) EIS plots of the Pd-MoS_2 and MoS_2 electrocatalysts. (**f**) Durability assessment at 10 mA cm^{-2} of the Pd-MoS_2 catalyst over 18 h.

Figure 7 illustrates the methanol-mediated hydrogen evolution reaction (MM-HER) of Pd-MoS_2 and MoS_2 catalysts. Figure 7a shows the LSV results of Pd-MoS_2 and MoS_2 electrocatalysts in 1 M methanol + 1 M KOH at 5 mV s^{-1}. The MM-HER process illustrated in Figure 7a demonstrates that the Pd-MoS_2 catalyst offers superior performance compared to pure MoS_2. Further, it is also observed that nanomaterial modifications using Pd are important for developing efficient and cost-effective Pd-MoS_2 catalysts for MM-HER [51]. The LSV plots of MoS_2 and Pd-MoS_2 catalysts reveal a substantial understanding of the electrocatalytic activity during MM-HER at 5 mV s^{-1}. Figure 7b displays an overpotential plot of the Pd-MoS_2 and MoS_2 electrocatalysts at −10 mA cm^{-2} for MM-HER. It is observed that the Pd-MoS_2 electrocatalyst divulges a lesser overpotential value of 224.6 mV compared with the pure MoS_2 catalyst of 251.8 mV at −10 mA cm^{-2}. Further, the decline in overpotential from 251.8 mV of the pure MoS_2 catalyst to 224.6 mV of Pd-doped MoS_2 can attain the same reaction rate with less energy input because of a vast surface area and excellent conductivity. The improvement in electrocatalytic performance in 1 M methanol + 1 M KOH during MM-HER is due to Pd doping, which can be attributed to several factors such as increased electronic conduction, better active site availability on the Pd-MoS_2 surface, and synergistic effects between Pd and MoS_2, developing a cost-effective and efficient MM-HER catalyst for clean and green hydrogen production [52]. Figure 7c

exhibits the Tafel curves of Pd-MoS_2 and MoS_2 catalysts for MM-HER. Interestingly, the Pd-MoS_2 catalyst exhibits a low Tafel curve of 113 mV dec^{-1} comparable to the MoS_2 catalyst of 115 mV dec^{-1}. It is detected that the Pd-doped MoS_2 catalyst displays a slightly lower Tafel slope compared to the pure MoS_2 catalyst, demonstrating upgraded charge transfer kinetics and overall catalytic effectiveness in the methanol-mediated hydrogen evolution reaction for hydrogen generation. On the other hand, the importance of Tafel slope enhancement lies in faster reaction kinetics, higher energy efficiency, and greater commercial feasibility, which makes the Pd-MoS_2 catalyst an auspicious candidate for MM-HER application [46]. Moreover, a low Tafel slope of the Pd-MoS_2 catalyst corresponds to the lower overpotential essential for achieving a −10 mA cm^{-2}, as exposed in Figure 7c, representing less energy consumption for hydrogen generation, which offers methanol-mediated hydrogen generation process more energy efficient. Further, Figure 7d displays the LSV plots of the Pd-MoS_2 at 5 mV s^{-1} without and with methanol-mediated HER. Interestingly, it is observed that the overpotentials are 269.6 mV, and 224.6 mV at −10 mA cm^{-2} during without and with methanol-mediated HER, respectively. Figure 7e explores the EIS spectra of the MoS_2 and Pd-MoS_2 at respective overpotentials of MM-HER, which portrays the low series and charge-transfer resistance of the Pd-MoS_2 compared with MoS_2. Figure 7f unveils a chronopotentiometry test to uncover the stability test of the Pd-MoS_2 during MM-HER at −10 mA cm^{-2}. It is observed that the stability of the Pd-MoS_2 catalyst slightly increased from 195.9 mV to 228.5 mV −10 mA cm^{-2}. Fascinatingly, the Pd-MoS_2 electrocatalyst exhibits unique nanolayered morphology, which delivers a high transport of charge carriers and plenty of active sites on the catalyst surface, facilitating effective mass transport and enhanced exposure of active sites with the 1 M KOH and 1 M methanol electrolyte ions, leading to excellent stability [53].

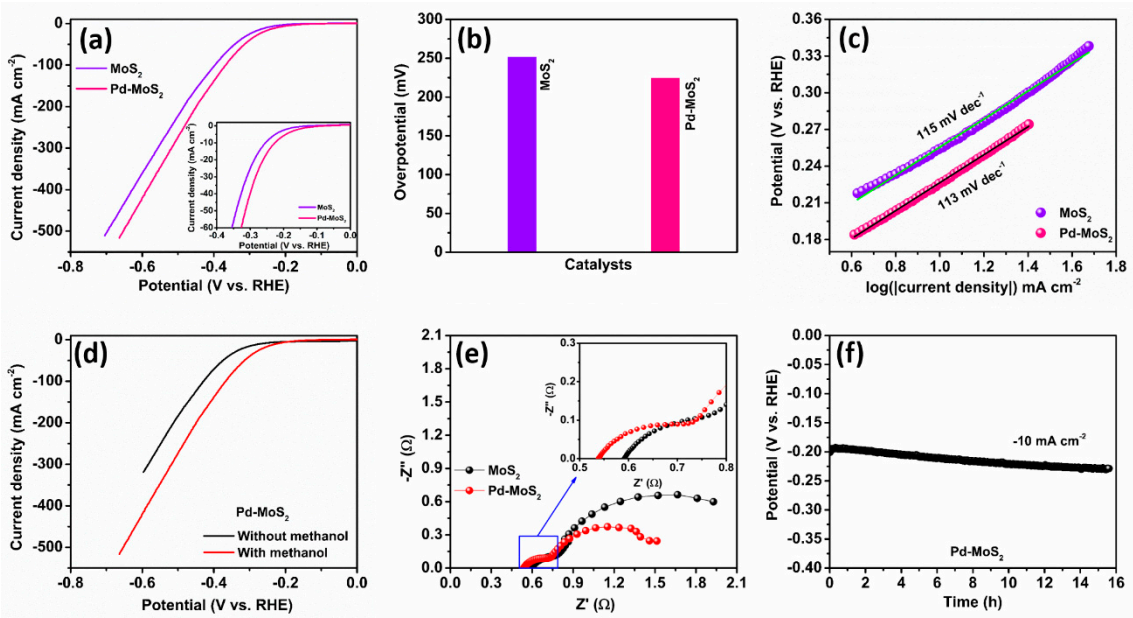

Figure 7. Electrocatalytic activities of methanol-mediated HER. (**a**) LSV results, (**b**) overpotential graphs, and (**c**) Tafel graphs of Pd-MoS_2 and MoS_2 electrocatalysts. (**d**) LSV curves of the Pd-MoS_2 without and with methanol. (**e**) EIS plots of the Pd-MoS_2 and MoS_2 electrocatalysts. (**f**) Durability examination at −10 mA cm^{-2} for the Pd-MoS_2 catalyst during 18 h.

Figure 8a–f illustrate the methanol-mediated overall water splitting (MM-OWS) of Pd-MoS_2||Pd-MoS_2 and MoS_2||MoS_2 cells. Figure 8a shows the LSV results of the MoS_2||MoS_2 cell and Pd-MoS_2||Pd-MoS_2 cell for MM-OWS in a 1 M KOH + 1 M methanol electrolyte at 5 mV s^{-1}. The catalytic performances of Pd-MoS_2||Pd-MoS_2 and MoS_2||MoS_2 are assessed

by investigating the cell potential at 10 mA cm^{-2} in the LSV plot. Further, it is seen from LSV plots that the Pd doping ominously enriches the electrocatalytic activities of the Pd-MoS_2||Pd-MoS_2 cell compared with the MoS_2||MoS_2 cell in methanol-mediated overall water splitting (MM-OWS). Figure 8b displays the cell potentials of the Pd-MoS_2||Pd-MoS_2 cell and MoS_2||MoS_2 cell for MM-OWS at 10 mA cm^{-2}. Fascinatingly, the lower potential of the Pd-MoS_2||Pd-MoS_2 cell (1.581 V) compared to the MoS_2||MoS_2 cell (1.648 V) may be due to the alterations of electronic properties, synergistic, and adsorption effects introduced by Pd doping, which makes the Pd-MoS_2||Pd-MoS_2 cell a more efficient for methanol-mediated overall water splitting. Further, Figure 8c illustrates the LSV curves of the Pd-MoS_2||Pd-MoS_2 cell at 5 mV s^{-1} without and with methanol-mediated OWS. Interestingly, it is observed that the potentials of the Pd-MoS_2||Pd-MoS_2 cell are 1.656 V and 1.581 V without and with methanol-mediated HER at 10 mA cm^{-2}, respectively. Figure 8d,e show the CV plots of the non-Faradic region of the MoS_2 and Pd-doped MoS_2 catalysts to evaluate a double-layer capacitance (C_{dl}) in 1 M KOH + 1 M methanol. Figure 8f,g elucidate the C_{dl} of MoS_2 and Pd-doped MoS_2 catalysts, which were evaluated by the CV plots of the non-Faradic region (Figure 8d,e). It is detected that the Pd-MoS_2 divulges a high C_{dl} of 55.1 mF compared to the MoS_2 of 45.7 mF. Figure 8h reveals the stability test of the Pd-MoS_2||Pd-MoS_2 cell for MM-OWS throughout 18 h at 10 mA cm^{-2}. In addition, it offers a cherished understanding of the stability of the Pd-MoS_2||Pd-MoS_2 cell in MM-OWS, signifying the capability for long-term use over 18 h. The stability at 10 mA cm^{-2} supports the Pd-MoS_2||Pd-MoS_2 cell's appropriateness for enduring use in electrochemical methanol-mediated overall water splitting application. Moreover, the strength of the Pd-MoS_2||Pd-MoS_2 cell at 10 mA cm^{-2} for an extended period is decisive for hands-on applications of MM-OWS, as it suggests the cell can reliably operate under typical conditions without significant degradation. This has implications for the Pd-MoS_2||Pd-MoS_2 cell's longevity, cost-effectiveness, and commercial viability. Moreover, the excellent methanol-mediated overall water splitting performances of the Pd-MoS_2 catalyst are due to numerous factors, such as a vast surface area due to a layered structure for the adsorption and reaction of methanol and protons. Furthermore, Pd doping improves the catalytic activity by facilitating the dehydrogenation and adsorption of methanol and improving the hydrogen adsorption sites and the synergistic effects between the MoS_2 and Pd, increasing the electrical conductivity, which is crucial for efficient electron transfer during both reactions in MM-OER and MM-HER. Figure 8i portrays the schematic illustration of the operation of the Pd-MoS_2||Pd-MoS_2 cell for methanol-mediated overall water splitting. In the Pd-MoS_2||Pd-MoS_2 cell configuration, the anodic side facilitates the MM-OER reaction, generating electrons and protons; however, the cathodic electrode offers the reaction mechanism for MM-HER.

Furthermore, Table 1 shows the assessment of the electrocatalytic activities of MoS_2-based catalysts in OER, HER, and OWS. The Co@NC@MoS_2 catalyst displays a 297 mV overpotential and elucidates excellent constancy throughout 10 h in 1.0 M KOH at 10 mA cm^{-2} for oxygen evolution reaction (OER) in 1 M KOH or 0.5 M H_2SO_4 [54]. Moreover, the MoS_2@Co catalyst reveals a 370 mV overpotential, exposing brilliant reliability over 20 h at 10 mA cm^{-2} for OER [55]. Further, the CoMnCr LDH@MoS_2/NF catalyst divulges a 229 mV overpotential with outstanding stability for 24 h at 10 mA cm^{-2} for OER [56]. Also, the MoS_2@CoO catalyst discloses a 325 mV overpotential and good durability for 1000 cycles at 10 mA cm^{-2} for OER [57]. In addition, the Co-Sv-MoS_2 catalyst unveils 190 mV overpotential and robustness for 12 h at 10 mA cm^{-2} for OER [58]. Interestingly, the RuO_2 catalyst uncovers 199 mV overpotential and strength only for 5.5 h at 10 mA cm^{-2} for OER [59]. Remarkably, the LSC/MoS_2 catalyst exposes a 284 mV overpotential and long life over 1 h at −10 mA cm^{-2} for the hydrogen evolution reaction (HER) [60]. Curiously, the 2H-MoS_2 catalyst illustrates a 369 mV overpotential and robustness over 24 h at

−10 mA cm^{-2} for HER [61]. In addition, the Ni/MoS_2-1000 catalyst elucidates a 229 mV overpotential and toughness over 2000 cycles at −10 mA cm^{-2} for HER [62]. Furthermore, the MoS_2 catalyst exposes nearly a 240 mV overpotential and robustness for ~47 h at −10 mA cm^{-2} for HER [63]. Likewise, the SL-MoS_2/CP catalyst reveals the overpotential of 267 mV at −10 mA cm^{-2} and long-term stability for 12 h for HER [64]. Remarkably, the Pt/C (20 wt.%) catalyst reveals a 43 mV overpotential and long endurance for 5000 cycles at −10 mA cm^{-2} for HER [65]. Further, Fe-(NiS_2/MoS_2)/CNT||Fe-(NiS_2/MoS_2)/CNT reveals a 1.51 V potential and durability over 8 h at 10 mA cm^{-2} during overall water splitting (OWS) [66]. Additionally, $CoFe_2O_4$@MoS_2/CC||$CoFe_2O_4$@MoS_2/CC displays 1.54 V potential and cell life for 12 h at 20 mA cm^{-2} during overall water splitting (OWS) [67]. Interestingly, NiCo-MoS_2-CW||NiCo-MoS_2-CW illustrates a 1.69 V potential at 50 mA cm^{-2} during OWS [68]. Fascinatingly, Co_9S_8/MnS/MoS_2/NF-2||Co_9S_8/MnS/MoS_2/NF-2 elucidates a 1.55 V potential and feasible operation for 26 h at 2.0 V during OWS [69]. Further, 1T-MoS_2/Ni_3S_2/LDH||1T-MoS_2/Ni_3S_2/LDH elucidates a potential of 1.55 V and longstanding operation for 20 h during OWS [70]. Interestingly, the present work (Pd-MoS_2||Pd-MoS_2 catalyst) illustrates 133 mV and a 224.6 mV overpotential and stability over 18 h and 16 h during a methanol-mediated OER and methanol-mediated HER. Additionally, the present work (Pd-MoS_2||Pd-MoS_2 cell) reveals a 1.581 V potential and working strength of 18 h during methanol-mediated OWS. Therefore, it is concluded that the Pd-doped MoS_2 catalyst reveals excellent electrocatalytic properties in MM-OER, MM-HER, and MM-OWS.

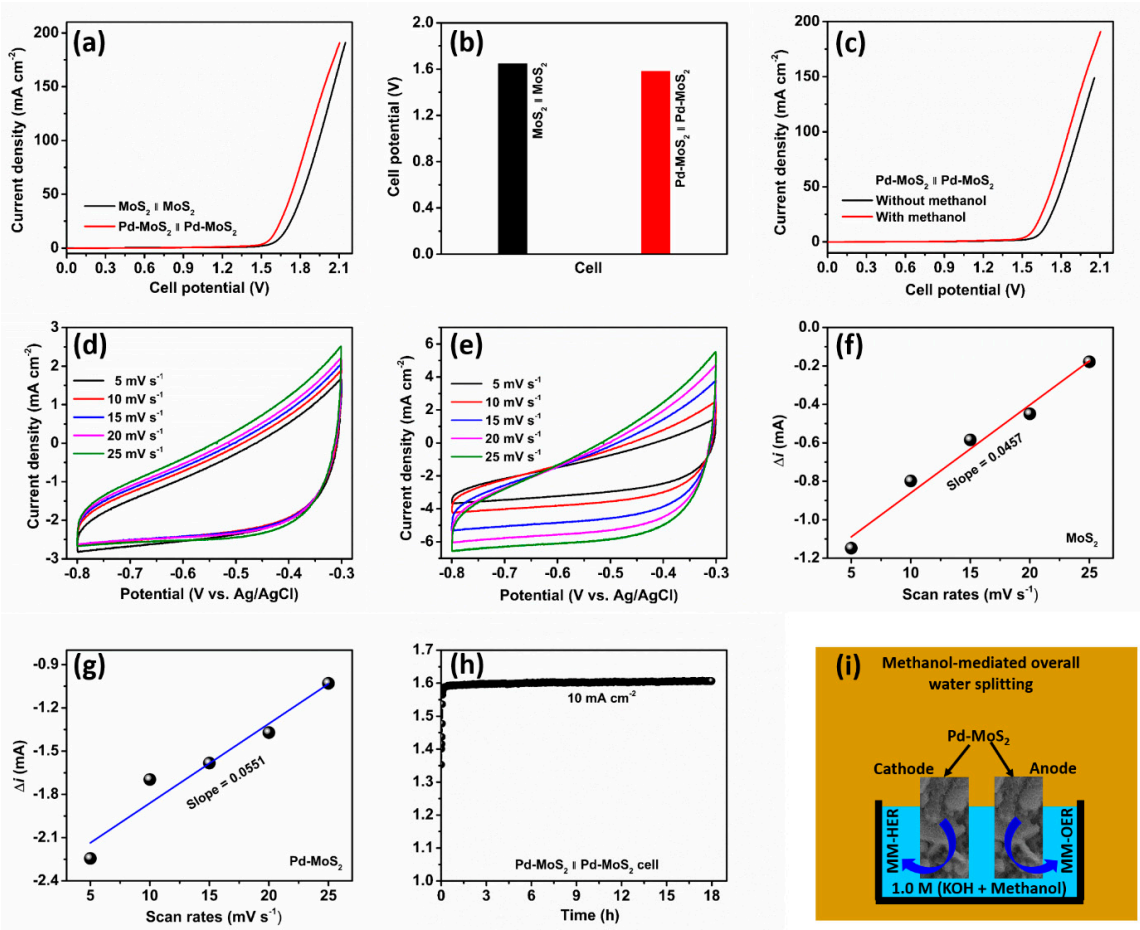

Figure 8. Electrocatalytic activities of methanol-mediated OWS. (**a**) LSV curves, (**b**) cell potentials of the MoS_2||MoS_2 and Pd-MoS_2||Pd-MoS_2, and (**c**) LSV curves of the Pd-MoS_2||Pd-MoS_2 without and with methanol. CV curves of the (**d**) MoS_2 and (**e**) Pd-MoS_2. C_{dl} graphs of the (**f**) MoS_2 and (**g**) Pd-doped MoS_2 catalysts. (**h**) Steadiness test of the Pd-MoS_2||Pd-MoS_2 over 18 h at 10 mA cm^{-2}. (**i**) Graphic drawing of the Pd-MoS_2||Pd-MoS_2 cell configuration in methanol-mediated overall water splitting.

Table 1. Assessment of the electrocatalytic properties of MoS_2-based catalysts in OER, HER, and OWS.

S. No.	Catalysts	Electrolyte	Overpotential (10 mA cm^{-2})	Stability (10 mA cm^{-2})	Ref.
Oxygen evolution reaction (OER)/Methanol-mediated OER (MM-OER)					
1	Co@NC@MoS_2	1.0 M KOH	297 mV	10 h	[54]
2	MoS_2@Co	1.0 M KOH	370 mV	20 h	[55]
3	CoMnCr LDH@MoS_2/NF	1.0 M KOH	229 mV	24 h	[56]
4	MoS_2@CoO-coated carbon cloth	1.0 M KOH	325 mV	1000 cycles	[57]
5	Co-Sv-MoS_2	1.0 M KOH	190 mV	12 h	[58]
6	RuO_2	0.5 M H_2SO_4	199 mV	~5.5 h	[59]
7	Pd-MoS_2 (MM-OER)	1.0 M KOH + 1.0 M Methanol	133 mV	18 h	This work
Hydrogen evolution reaction (HER)/Methanol-mediated HER (MM-HER)					
8	LSC/MoS_2	1.0 M KOH	284 mV	1 h	[60]
9	2H-MoS_2	0.5 M H_2SO_4	369 mV	24 h	[61]
10	Ni/MoS_2-1000	0.5 M H_2SO_4	229 mV	2000 cycles	[62]
11	MoS_2	0.5 M H_2SO_4	~240 mV	~47 h	[63]
12	SL-MoS_2/CP	0.5 M H_2SO_4	267 mV	12 h	[64]
13	Pt/C (20 wt.%)	1.0 M KOH	43 mV	5000 cycles	[65]
14	Pd-MoS_2 (MM-HER)	1.0 M KOH + 1.0 M Methanol	224.6 mV	16 h	This work
Overall water splitting (OWS)/Methanol-mediated OWS (MM-OWS)					
15	Fe-(NiS_2/MoS_2)/CNT‖Fe-(NiS_2/MoS_2)/CNT	1.0 M KOH	1.51 V	8 h	[66]
16	$CoFe_2O_4$@MoS_2/CC‖$CoFe_2O_4$@MoS_2/CC	1.0 M KOH	1.54 V	12 h @20 mA cm^{-2}	[67]
17	NiCo-MoS_2-CW‖NiCo-MoS_2-CW	1.0 M KOH	1.69 V @50 mA cm^{-2}	--	[68]
18	Co_9S_8/MnS/MoS_2/NF-2‖Co_9S_8/MnS/MoS_2/NF-2	1.0 M KOH	1.55 mV	26 h @2.0 V	[69]
19	1T-MoS_2/Ni_3S_2/LDH‖1T-MoS_2/Ni_3S_2/LDH	1.0 M KOH	1.55 mV	20 h	[70]
20	Pd-MoS_2‖Pd-MoS_2 (MM-OWS)	1.0 M KOH + 1.0 M Methanol	1.581 V cell potential	18 h	This work

3. Synthesis Method

All the chemicals used were purchased from Sigma Aldrich, Seoul, Korea. This study synthesized Pd-doped MoS_2 and MoS_2 using a solvothermal procedure. Initially, 30 mL of ethanol and 30 mL of deionized water were dissolved in a 100 mL glass beaker to prepare the solvent. Subsequently, 16 mg of C_2H_5NS and 4 mmol of $Na_2MoO_2 \cdot 2H_2O$ were added to the solvent and blended using a magnetic stirrer. A Pd solution was obtained by melting 2 mg of $PdCl_2$ in 20 mL of the solvent mixture (10 mL deionized water and 10 mL ethanol) under sonication and magnetic stirring for several hours until it dissolved. While stirring the initial mixture, 1 mL of Pd solution was slowly added to the molybdenum and sulfur precursor solution. Further, the whole solution was then moved into a 100 mL autoclave. The 2 cm × 3 cm slice of cleaned Ni-foam substrate was placed into the autoclave containing

the above solution. The Teflon autoclave was closed and preserved in an oven for 18 h at 180 °C to facilitate the synthesis. The Ni-foam, now deposited with Pd-doped MoS_2, was cleaned carefully with ethanol and water to exclude undesired residues. Ultimately, the cleaned Ni-foam was dehydrated in a vacuum oven at 90 °C for 15 h. Likewise, MoS_2 was prepared through the above process without a Pd precursor.

The Pd-MoS_2 shape was precisely studied by the scanning electron microscope (SEM) [S-4800 HITACHI, Ltd., Tokyo, Japan]. Furthermore, the structure, morphology, and Pd, S, and Mo elements of the Pd-MoS_2 were analyzed using TEM, HRTEM, and color mapping by JEOL [JEM-2100F, JEOL Ltd., Tokyo, Japan]. The crystal nanostructures of the Pd-doped MoS_2 and MoS_2 were analyzed by X-ray diffraction (XRD) with a PANalytical apparatus. Additionally, X-ray photoelectron spectroscopy (XPS) was employed to inspect the chemical properties of the Pd-doped MoS_2 using a Thermo Scientific system (Winsford, UK) furnished with the source of an Al K-alpha X-ray (400 μm). In addition, the methanol-mediated oxygen evolution reaction (MM-OER), methanol-mediated hydrogen evolution reaction (MM-HER), and methanol-mediated overall water splitting (MM-OWS) of the Pd-MoS_2 and MoS_2 electrocatalysts were systematically inspected via the electrochemical VersaSTAT3 (Princeton Applied Research) workstation. The MM-OER and MM-HER performances of the Pd-MoS_2 and MoS_2 catalysts were studied in a three-electrode configuration in a 1.0 M methanol + 1.0 M KOH. The MoS_2 and Pd-MoS_2 catalysts, graphite sheet, and Ag/AgCl were employed as working, counter, and reference electrodes, respectively. Further, the MM-OWS was inspected in the two-electrode configuration in 1.0 M KOH + 1.0 M methanol, in which MoS_2 or Pd-MoS_2 were utilized in both cathode and anode electrodes. The linear sweep voltammetry (LSV) of the Pd-MoS_2 and MoS_2 catalysts were examined at 5 mV s^{-1}. In addition, the Tafel graphs of the Pd-MoS_2 and MoS_2 catalysts were evaluated via LSV results, by applying $\eta = a + b \log j$, where b is the Tafel slope, j is the current density, a is the transfer coefficient, and η is the overpotential. The observed potential vs. Ag/AgCl was changed in the reversible hydrogen electrode (RHE) using $E_{RHE} = E^{\circ}_{Ag/AgCl} + E_{Ag/AgCl} + 0.059 \times pH$.

4. Conclusions

In conclusion, this paper explored the potential of palladium (Pd) doping in MoS_2 for enhancing catalytic performances in methanol-mediated overall water splitting. The Pd-MoS_2 catalyst highlights several significant advancements and insights, including enhanced electrocatalytic performances and strength. The Pd doping in MoS_2 shows small Tafel slopes and low overpotential in MM-OER and MM-HER. Further, the Pd-MoS_2||Pd-MoS_2 cell depicts low cell potential and brilliant robustness over 18 h at 10 mA cm^{-2}. Consequently, it is anticipated that this approach offers a promising route toward practical and sustainable hydrogen generation because of the unique properties of the Pd-MoS_2 electrocatalyst and the beneficial effects of methanol in KOH electrolytes.

Author Contributions: Conceptualization, R.K.M.; Methodology, A.M.T. and S.M.M.; Formal analysis, A.M.T., S.M.M. and R.K.M.; Investigation, A.M.T., S.M.M. and R.K.M.; Data curation, A.M.T. and S.M.M.; Writing—original draft, A.M.T.; Writing—review & editing, A.M.T., R.K.M., W.J. and J.C.S.; Visualization, A.M.T., R.K.M. and W.J.; Supervision, R.K.M., W.J. and J.C.S.; Project administration, W.J. and J.C.S.; Funding acquisition, J.C.S. All authors have read and agreed to the published version of the manuscript.

Funding: This work was supported by the Technology Innovation Program (RS-2023-00235844, Development of nano-structured materials and devices for super steep subthreshold swing) funded By the Ministry of Trade, Industry & Energy (MOTIE, Korea) (1415187621).

Data Availability Statement: The original contributions presented in this study are included in the article. Further inquiries can be directed to the corresponding author.

Conflicts of Interest: The authors declare no conflict of interest.

References

1. Kumari, R.; Sammi, A.; Srivastava, A.; Azad, U.P.; Chandra, P. Emerging 3D nanomaterials as electrocatalysts for water splitting reactions. *Int. J. Hydrog. Energy* **2024**, *74*, 214–231. [CrossRef]
2. Imran, S.; Hussain, M. Emerging trends in water splitting innovations for solar hydrogen production: Analysis, comparison, and economical insights. *Int. J. Hydrog. Energy* **2024**, *77*, 975–996. [CrossRef]
3. Jin, C.; Zhang, Z.; Gui, L.; Zeng, X. 2D MXene-derived 3D TiO_2-$NiCoP_x$ hierarchical heterostructures for efficient water splitting. *J. Alloys Compd.* **2024**, *1002*, 175492. [CrossRef]
4. Salah, B.; Abdelgawad, A.; Lu, Q.; Ipadeola, A.K.; Luque, R.; Eid, K. Synergistically interactive MnFeM (M = Cu, Ti, and Co) sites doped porous g-C_3N_4 fiber-like nanostructures for an enhanced green hydrogen production. *Green Chem.* **2023**, *25*, 6032–6040. [CrossRef]
5. Abdelgawad, A.; Salah, B.; Lu, Q.; Abdullah, A.M.; Chitt, M.; Ghanem, A.; Al-Hajri, R.S.; Eid, K. Template-free synthesis of M/g-C_3N_4 (M = Cu, Mn, and Fe) porous one-dimensional nanostructures for green hydrogen production. *J. Electroanal. Chem.* **2023**, *938*, 117426. [CrossRef]
6. Mushtaq, M.A.; Ahmad, M.; Shaheen, A.; Mehmood, A.; Yasin, G.; Arif, M.; Ali, Z.; Li, P.; Hussain, S.N.; Tabish, M.; et al. Advancing the development of hollow micro/nanostructured materials for electrocatalytic water splitting: Current state, challenges, and perspectives. *ACS Mater. Lett.* **2024**, *6*, 3090–3111. [CrossRef]
7. Kulkarni, R.; Lingamdinne, L.P.; Koduru, J.R.; Karri, R.R.; Chang, Y.-Y.; Kailasa, S.K.; Mubarak, N.M. Recent advanced developments and prospects of surface functionalized MXenes-based hybrid composites toward electrochemical water splitting applications. *ACS Mater. Lett.* **2024**, *6*, 2660–2686. [CrossRef]
8. Lu, L.; Gu, Y.; Guo, W.; Lu, F.; Li, Y. Extrasmall ligand-free Pt nanoparticles as dual-function catalysts for methanol-assisted water splitting systems. *ACS Appl. Nano Mater.* **2022**, *5*, 4222–4229. [CrossRef]
9. Wei, X.; Wang, S.; Hua, Z.; Chen, L.; Shi, J. Metal-organic framework nanosheet electrocatalysts for efficient H_2 production from methanol solution: Methanol-assisted water splitting or methanol reforming? *ACS Appl. Mater. Interfaces* **2018**, *10*, 25422–25428. [CrossRef] [PubMed]
10. Li, M.; Duanmu, K.; Wan, C.; Cheng, T.; Zhang, L.; Dai, S.; Chen, W.; Zhao, Z.; Li, P.; Fei, H.; et al. Single-atom tailoring of platinum nanocatalysts for high-performance multifunctional electrocatalysis. *Nat. Catal.* **2019**, *2*, 495–503. [CrossRef]
11. Li, H.; Zhang, X.; Sun, Z.; Ma, W. Rapid screening of bimetallic electrocatalysts using single nanoparticle collision electrochemistry. *J. Am. Chem. Soc.* **2022**, *144*, 16480–16489. [CrossRef] [PubMed]
12. Chen, H.; Wang, Y.; Zhou, S.; Li, N.; Liu, X.; Abdukayum, A.; Zhang, L.; Hu, G. MoS_2-decorated ordered macroporous $Fe_2Mo_3O_8/MoO_2$ with heterogeneous structure as bifunctional electrocatalyst for efficient overall water splitting. *Ceram. Int.* **2024**, *50*, 16714–16721. [CrossRef]
13. Zhu, J.; Xia, L.; Yu, R.; Lu, R.; Li, J.; He, R.; Wu, Y.; Zhang, W.; Hong, X.; Chen, W.; et al. Ultrahigh stable methanol oxidation enabled by a high hydroxyl concentration on Pt clusters/MXene interfaces. *J. Am. Chem. Soc.* **2022**, *144*, 15529–15538. [CrossRef] [PubMed]
14. Pan, J.; Liu, X.; Ji, H.; Zhu, Y.; Zhuang, Y.; Chen, K.; Sun, N.; Liu, Y.; Lei, Y.; Wang, K.; et al. The strategies to improve TMDs represented by MoS_2 electrocatalytic oxygen evolution reaction. *Chin. Chem. Lett.* **2024**, *35*, 109515. [CrossRef]
15. Jiang, R.; Xiao, M.; Zhu, H.; Zang, X.; Zhao, D.; Zhu, J.; Long, Y.; Wang, Q. Intriguing and boosting molybdenum sulfide (MoS_2)-based materials for decontamination and purification of wastewater/seawater: An upgraded review. *Sep. Purif. Technol.* **2024**, *351*, 128063. [CrossRef]
16. Tian, L.; He, C.; Hu, J.; Yang, J.; Li, X.; Chen, Z. Electronic and optical properties and electrocatalytic water splitting in a graphene/MoS_2 heterojunction. *Phys. B* **2024**, *685*, 416062. [CrossRef]
17. Anushya, G.; Benjamin, M.; Sarika, R.; Pravin, J.C.; Sridevi, R.; Nirmal, D. A review on applications of molybdenum disulfide material: Recent developments. *Micro Nanostruct.* **2024**, *186*, 207742. [CrossRef]
18. Ma, J.; Wang, X.; Li, H.; Yang, D.; Fan, J.; Liu, Y. Boosting photocatalytic overall water splitting performance by dual-metallic single Ni and Pd atoms decoration of MoS_2: A DFT study. *J. Alloys Compd.* **2024**, *991*, 174530. [CrossRef]
19. Khanlary, M.R.; Parhizkari, M.; Heydari, N. Structural and optical properties of 1T-MoS_2/MoO_3 thin films prepared by spray pyrolysis method. *Phys. B* **2024**, *680*, 415837. [CrossRef]
20. Aliyar, T.; Ma, H.; Krishnan, R.; Singh, G.; Chong, B.Q.; Wang, Y.; Verzhbitskiy, I.; Wong, C.P.Y.; Goh, K.E.J.; Shen, Z.X.; et al. Symmetry breaking and spin-orbit coupling for individual vacancy-induced in-gap states in MoS_2 monolayers. *Nano Lett.* **2024**, *24*, 2142–2148. [CrossRef]

21. Mathew, R.; Ajayan, J. Material processing, performance and reliability of MoS_2 field effect transistor (FET) technology- A critical review. *Mater. Sci. Semicond. Process.* **2023**, *160*, 107397. [CrossRef]
22. Le, K.T.; Pham, N.N.T.; Liao, Y.-S.; Ranjan, A.; Lin, H.-Y.; Chen, P.-H.; Nguyen, H.; Lu, M.Y.; Lee, S.G.; Wu, J.M. Piezoelectricity of strain-induced overall water splitting of $Ni(OH)_2/MoS_2$ heterostructure. *J. Mater. Chem. A* **2023**, *11*, 3481–3492. [CrossRef]
23. Ding, E.-X.; Liu, P.; Yoon, H.H.; Ahmed, F.; Du, M.; Shafi, A.M.; Mehmood, N.; Kauppinen, E.I.; Sun, Z.; Lipsanen, H. Highly sensitive MoS_2 photodetectors enabled with a dry-transferred transparent carbon nanotube electrode. *ACS Appl. Mater. Interfaces* **2023**, *15*, 4216–4225. [CrossRef] [PubMed]
24. Im, H.; Kim, J.; Kim, J.; Kim, S. Scalable bilayer MoS_2-based vertically inverted p-i-n light-emitting diodes. *Adv. Mater. Interfaces* **2023**, *11*, 2300319. [CrossRef]
25. Hu, B.; Wu, Y.; Wang, K.; Guo, H.; Lei, Z.; Liu, Z.; Wang, L. Gram-scale mechanochemical synthesis of atom-layer MoS_2 semiconductor electrocatalyst via functionalized graphene quantum dots for efficient hydrogen evolution. *Small* **2023**, *20*, 2305344. [CrossRef] [PubMed]
26. Man, P.; Jiang, S.; Leung, K.H.; Lai, K.H.; Guang, Z.; Chen, H.; Huang, L.; Chen, T.; Gao, S.; Peng, K.; et al. Salt-induced high-density vacancy-rich 2D MoS_2 for efficient hydrogen evolution. *Adv. Mater.* **2024**, *36*, 2304808. [CrossRef] [PubMed]
27. Chen, P.S.; Hu, Y.; Li, S.; Mazurkiewicz-Pawlicka, M.; Małolepszy, A. Preparation of a MoS_2/carbon nanotube nanocomposite by hydrothermal method for supercapacitor. *Int. J. Electrochem. Sci.* **2024**, *19*, 100523. [CrossRef]
28. Sun, K.; Guo, H.; Feng, C.; Tian, F.; Zhao, X.; Wang, C.; Chai, Y.; Liu, B.; Mintova, S.; Liu, C. One–pot solvothermal preparation of the porous $NiS_2//MoS_2$ composite catalyst with enhanced low-temperature hydrodesulfurization activity. *J. Colloid Interface Sci.* **2024**, *659*, 650–664. [CrossRef] [PubMed]
29. Wang, Y.; Zhai, W.; Ren, Y.; Zhang, Q.; Yao, Y.; Li, S.; Yang, Q.; Zhou, X.; Li, Z.; Chi, B.; et al. Phase-controlled growth of 1T-MoS_2 nanoribbons on 1H-MoS_2 nanosheets. *Adv. Mater.* **2024**, *36*, 2307269. [CrossRef] [PubMed]
30. Alrowaily, A.W.; Alyousef, H.A.; Alotaibi, B.; Alotiby, M.F.; Al-Sehemi, A.G.; Ahmad, K.; Henaish, A.; Al-Zahrani, F.A. Facile synthesis of $CuMn_2O_4$ nanoparticle supported on MoS_2 nanorods via hydrothermal route for supercapacitor application. *Mater. Chem. Phys.* **2024**, *322*, 129517. [CrossRef]
31. Liang, S.; Zheng, J.; Song, N.; Wang, X.; Tu, B.; Xu, J. Accelerated confined mass transfer of MoS_2 1D nanotube in photo-assisted metal-air batteries. *Adv. Mater.* **2024**, *36*, 2307790. [CrossRef] [PubMed]
32. Yang, L.; Yuan, X.; Dong, Y.; Qian, S.; Zhu, C. Hierarchical nanowires of MoS_2@transition metal sulfide heterostructures for efficient electrocatalytic hydrogen evolution reaction. *J. Electroanal. Chem.* **2024**, *964*, 118342. [CrossRef]
33. Wen, Y.; Li, D.; Jin, D.; Jin, H. Comparative study on gas-sensing properties of amorphous MoS_2 nanoparticles and crystalline MoS_2 nanoflowers. *Mater. Sci. Semicond. Process.* **2024**, *172*, 108077. [CrossRef]
34. Wang, S.; White, J.; Li, M.; Azam, A.; Yang, J.; Zu, X.; Qiao, L.; Reece, P.; Stride, J.; Zhang, S.; et al. Size control of MoS_2 quantum dots by varying the crystallographic orientation of sapphire substrates. *Mater. Today Chem.* **2023**, *35*, 101887. [CrossRef]
35. Mouloua, D.; LeBlanc-Lavoie, J.; Pichon, L.; Rajput, N.S.; Marssi, M.E.; Jouiad, M.; El Khakani, M.A. Tuning the optoelectronic properties of pulsed laser deposited "3D"-MoS_2 films via the degree of vertical alignment of their constituting layers. *Adv. Opt. Mater.* **2024**, *12*, 2302966. [CrossRef]
36. Zhu, W.; Zhao, J.; Tao, X. MoS_2-carbon based nanocomposites as anodes for lithium-ion batteries: A review. *J. Energy Storage* **2024**, *84*, 110934. [CrossRef]
37. Wang, W.; Tang, L.; Chen, C.; Wang, X.; Wang, Y.; Sun, W. Engineering Pt-S-Mo and Pd-S-Mo sites in hierarchical porous MoS_2 for boosted oxygen reduction activity in microbial fuel cell. *J. Power Sources* **2024**, *598*, 234143. [CrossRef]
38. Zhang, Y.; Zhang, R.; Guo, Y.; Li, Y.; Li, K. A review on MoS_2 structure, preparation, energy storage applications and challenges. *J. Alloys Compd.* **2024**, *998*, 174916. [CrossRef]
39. Cantarella, M.; Spanò, V.; Zimbone, M.; Giuffrida, F.; Lufrano, E.; Strano, V.; Franzò, G.; Sfuncia, G.; Nicotra, G.; Alberti, A.; et al. ZnO-MoS_2-PMMA polymeric nanocomposites: A harmless material for water treatment. *Mater. Today Chem.* **2024**, *36*, 101912. [CrossRef]
40. Singh, H.; Rathour, R.K.S.; Raj, S.; Bhattacharya, J. Environment friendly MOF-MoS_2 composite for Cr(VI) and Pb(II) capture from paint industry wastewater: Sequestration, regeneration and toxicity. *Inorg. Chim. Acta* **2024**, *570*, 122165. [CrossRef]
41. Ghosh, S.; Lai, J. An insight into the dual role of MoS_2-based nanocarriers in anticancer drug delivery and therapy. *Acta Biomater.* **2024**, *179*, 36–60. [CrossRef]
42. Lin, S.; Joshi, R.; Ganguly, A.; Barman, S.R.; Pal, A.; Kaswan, K.; Liu, K.; Nain, A.; Kao, F.; Lin, Z. Ultrasound-guided drug delivery system utilizing piezocatalytic MoS_2 nanomaterials for anti-inflammatory therapy. *Nano Energy* **2024**, *127*, 109732. [CrossRef]
43. Zhao, L.; Wang, Y.; Wen, G.; Zhang, X.; Huang, X. Ammonium-driven modulation of 1T-MoS_2 structure and composite with graphene: A pathway to high-performance lithium-ion battery anodes. *J. Colloid Interface Sci.* **2025**, *680*, 151–161. [CrossRef]
44. Li, B.; Jiang, L.; Li, X.; Ran, P.; Zuo, P.; Wang, A.; Qu, L.; Zhao, Y.; Cheng, Z.; Lu, Y. Preparation of monolayer MoS_2 quantum dots using temporally shaped femtosecond laser ablation of bulk MoS_2 targets in water. *Sci. Rep.* **2017**, *7*, 11182. [CrossRef]

45. Lai, B.; Singh, S.C.; Bindra, J.K.; Saraj, C.S.; Shukla, A.; Yadav, T.P.; Wu, W.; McGill, S.A.; Dalal, N.S.; Srivastava, A.; et al. Hydrogen evolution reaction from bare and surface-functionalized few-layered MoS_2 nanosheets in acidic and alkaline electrolytes. *Mater. Today Chem.* **2019**, *14*, 100207. [CrossRef]
46. Gupta, J.; Das, D.; Borse, P.H.; Sarada, B.V. In situ Pd-doped MoS_2 nanosheets as an HER electrocatalyst for enhanced electrocatalytic water splitting. *Sustain. Energy Fuels* **2024**, *8*, 1526–1539. [CrossRef]
47. Xuan, T.T.; Long, L.N.; Khai, T.V. Effect of reaction temperature and reaction time on the structure and properties of MoS_2 synthesized by hydrothermal method. *Vietnam J. Chem.* **2020**, *58*, 92–100. [CrossRef]
48. Zhang, H.; Lin, H.; Zheng, Y.; Hu, Y.; MacLennan, A. Understanding of the effect of synthesis temperature on the crystallization and activity of nano-MoS_2 catalyst. *Appl. Catal. B* **2015**, *165*, 537–546. [CrossRef]
49. Han, C.; Huang, G.; Zhu, D.; Hu, K. Facile synthesis of MoS_2/Fe_3O_4 nanocomposite with excellent Photo-Fenton-like catalytic performance. *Mater. Chem. Phys.* **2017**, *200*, 16–22. [CrossRef]
50. Wang, J.; Zhang, B.; Guo, W.; Wang, L.; Chen, J.; Pan, H.; Sun, W. Toward electrocatalytic methanol oxidation reaction: Longstanding debates and emerging catalysts. *Adv. Mater.* **2023**, *35*, 2211099. [CrossRef] [PubMed]
51. Yin, S.; Liu, S.; Wang, Z.; Xu, Y.; Li, X.; Wang, H.; Wang, L. Methanol-assisted energy-saving hydrogen production over defect-rich perforated PdIn bimetallene. *Chem. Eng. J.* **2022**, *435*, 134711. [CrossRef]
52. Li, B.; Qiao, S.; Zheng, X.; Yang, X.; Cui, Z.; Zhu, S.; Li, Z.; Liang, Y. Pd coated MoS_2 nanoflowers for highly efficient hydrogen evolution reaction under irradiation. *J. Power Sources* **2015**, *284*, 68–76. [CrossRef]
53. Yu, E.; Pan, Y. Enhancing the catalytic hydrogen evolution reaction (HER) of the defective borophene@Pt/Pd/MoS_2 heterojunction. *Int. J. Hydrog. Energy* **2024**, *50*, 920–931. [CrossRef]
54. Gaur, A.; Sachdeva, P.K.; Kumar, R.; Maruyama, T.; Bera, C.; Bagchi, V. Ultrathin MoS_2 wrapped N-doped carbon-coated cobalt nanospheres for OER applications. *Sustain. Energy Fuels* **2021**, *5*, 801–807. [CrossRef]
55. Cao, S.; Wu, W.; Liu, C.; Song, L.; Xu, Q.; Zhang, H.; Zhao, Y. Supramolecular macrocycle regulated single-atom MoS_2@Co catalysts for enhanced oxygen evolution reaction. *Energy Environ. Mater.* **2024**, *7*, e12702. [CrossRef]
56. Vedanarayanan, M.; Gopalakrishnan, S.M. Enhancement of hydrogen and oxygen evolution reaction efficiencies by coupling a MoS_2 nanoflower with a CoMnCr LDH nanocube on nickel foam. *Energy Fuels* **2023**, *37*, 12204–12214. [CrossRef]
57. Cheng, P.; Yuan, C.; Zhou, Q.; Hu, X.; Li, J.; Lin, X.; Wang, X.; Jin, M.; Shui, L.; Gao, X.; et al. Core-shell MoS_2@CoO electrocatalyst for water splitting in neural and alkaline solutions. *J. Phys. Chem. C* **2019**, *123*, 5833–5839. [CrossRef]
58. Ma, Y.; Leng, D.; Zhang, X.; Fu, J.; Pi, C.; Zheng, Y.; Gao, B.; Li, X.; Li, N.; Chu, P.K.; et al. Enhanced activities in alkaline hydrogen and oxygen evolution reactions on MoS_2 Electrocatalysts by in-plane sulfur defects coupled with transition metal doping. *Small* **2022**, *18*, 2203173. [CrossRef] [PubMed]
59. Zhao, Z.L.; Wang, Q.; Huang, X.; Feng, Q.; Gu, S.; Zhang, Z.; Xu, H.; Zeng, L.; Gu, M.; Li, H. Boosting the oxygen evolution reaction using defect-rich ultra-thin ruthenium oxide nanosheets in acidic media. *Energy Environ. Sci.* **2020**, *13*, 5143–5151. [CrossRef]
60. Zhao, Y.-N.; Sun, N.; Xu, S.; Min, S.; Dong, H.; Li, J.; Liu, C.; Chen, Z. An interface engineering strategy of MoS_2/perovskite oxide as a bifunctional catalyst to boost overall water splitting. *J. Mater. Chem. A* **2024**, *12*, 8757–8768. [CrossRef]
61. Guo, X.; Song, E.; Zhao, W.; Xu, S.; Zhao, W.; Lei, Y.; Fang, Y.; Liu, J.; Huang, F. Charge self-regulation in 1T'''-MoS_2 structure with rich S vacancies for enhanced hydrogen evolution activity. *Nat. Commun.* **2022**, *13*, 5954. [CrossRef] [PubMed]
62. Lu, X.; Sun, J.; Liu, Z.; Pan, Y.; Li, Y.; Zhang, D.; Lin, Y.; Qu, X. Scalable synthesis of hollow MoS_2 nanoparticles modified on porous Ni for improved hydrogen evolution reaction. *J. Electrochem. Soc.* **2021**, *168*, 056519. [CrossRef]
63. Kumar, M.; Nagaiah, T.C. A NiCu-MoS_2 electrocatalyst for pH-universal hydrogen evolution reaction and Zn-air batteries driven self-power water splitting. *J. Mater. Chem. A* **2023**, *11*, 18336–18348. [CrossRef]
64. Li, B.L.; Gong, C.-B.; Shen, W.; Peng, J.-D.; Zou, H.L.; Luo, H.Q.; Li, N.B. Engineering metallic MoS_2 monolayers with responsive hydrogen evolution electrocatalytic activities for enzymatic reaction monitoring. *J. Mater. Chem. A* **2021**, *9*, 11056–11063. [CrossRef]
65. Jiang, B.; Liu, S.; Cheng, L.; Zhou, L.; Cui, H.; Liu, M.; Wen, M.; Wang, C.; Wang, W.; Li, S.; et al. Mass synthesis of Pt/C catalysts with high Pt loading for low-overpotential hydrogen evolution. *Int. J. Hydrog. Energy* **2024**, *58*, 268–278. [CrossRef]
66. Li, C.; Liu, M.; Ding, H.; He, L.; Wang, E.; Wang, B.; Fan, S.; Liu, K. A lightly Fe-doped (NiS_2/MoS_2)/carbon nanotube hybrid electrocatalyst film with laser-drilled micropores for stabilized overall water splitting and pH-universal hydrogen evolution reaction. *J. Mater. Chem. A* **2020**, *8*, 17527–17536. [CrossRef]
67. Duan, Y.; Guo, Z.; Wang, T.; Zhang, J. Uniform anchoring of MoS_2 nanosheets on MOFs-derived $CoFe_2O_4$ porous nanolayers to construct heterogeneous structural configurations for efficient and stable overall water splitting. *J. Colloid Interface Sci.* **2025**, *680*, 541–551. [CrossRef] [PubMed]
68. Hu, M.; Qian, Y.; Zhang, R.; Guo, C.; Yang, L.; Li, L. Interfacial electronic modulation of NiCo decorated nano-flowered MoS_2 on carbonized wood as a remarkable bifunctional electrocatalyst for boosting overall water splitting. *J. Colloid Interface Sci.* **2024**, *677*, 729–738. [CrossRef]

69. Yan, R.; Luan, T.; Liu, Z.; Cao, Y.; Chi, K.; Yang, S.; Guo, X. Co_9S_8/MnS/MoS_2 heterostructure grown in situ on Ni foam as highly efficient electrocatalysts for overall water splitting. *Int. J. Hydrog. Energy* **2025**, *98*, 14–24. [CrossRef]
70. Liu, W.; Dong, J.; An, B.; Su, H.; Teng, Z.; Li, N.; Gao, Y.; Ge, L. Synergistic dual built-in electric fields in 1T-MoS_2/Ni_3S_2/LDH for efficient electrocatalytic overall water splitting reactions. *J. Colloid Interface Sci.* **2024**, *673*, 228–238. [CrossRef]